J. Fluid Mech. (2019), *vol.* 869, R6, doi:10.1017/jfm.2019.299

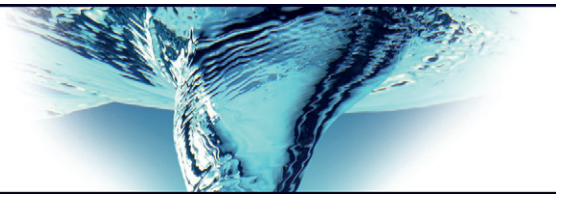

JFM RAPIDS
journals.cambridge.org/rapids

Fractal features of turbulent/non-turbulent interface in a shock wave/turbulent boundary-layer interaction flow

Yi Zhuang[1], **Huijun Tan**[1,†], **Weixing Wang**[1], **Xin Li**[1] **and Yunjie Guo**[1]

[1]Jiangsu Province Key Laboratory of Aerospace Power System, College of Energy and Power Engineering, Nanjing University of Aeronautics and Astronautics, Nanjing 210016, China

(Received 9 January 2019; revised 7 April 2019; accepted 8 April 2019;
first published online 29 April 2019)

Fractal features of the turbulent/non-turbulent interface (TNTI) in shock wave/turbulent boundary-layer interaction (SWBLI) flows are essential in understanding the physics of the SWBLI and the supersonic turbulent boundary layer, yet have received almost no attention previously. Accordingly, this study utilises a high spatiotemporal resolution visualisation technique, ice-cluster-based planar laser scattering (IC-PLS), to acquire the TNTI downstream of the reattachment in a SWBLI flow. Evolution of the fractal features of the TNTI in this SWBLI flow is analysed by comparing the parameters of the TNTI acquired in this study with those from a previous result (Zhuang *et al. J. Fluid Mech.*, vol. 843, 2018*a*).

Key words: fractals, turbulent boundary layers, wave–turbulence interactions

1. Introduction

Shock wave/turbulent boundary-layer interaction (SWBLI) phenomena are omnipresent in supersonic and transonic fight, playing a critical role in nearly all flow issues concerning high-speed applications (Dolling 2001). First observed by Ferri (1940), the SWBLI has attracted investigations from theoretical, experimental and numerical perspectives. Consequently, significant improvements in understanding various features of the phenomena, such as the general flow patterns, separation predictions, characters of flow-field unsteadiness, and flow control methods, have been achieved in past decades (Adamson Jr & Messiter 1980; Zheltovodov 1996; Dolling 2001; Smits & Dussauge 2006; Babinsky & Harvey 2011; Gaitonde 2015). As suggested by Dolling (2001), the investigation on SWBLI has entered an explanatory phase and thus requires new experimental tools and developments in numerical simulation. Additionally, features derived from new perspectives should be added to existing studies.

† Email address for correspondence: thj@263.net

Generally, turbulent flow is confined by irrotational flows. The sharp and irregularly wrinkled surface that divides fluids of these two states, first reported by Corrsin & Kistler (1954), is a vital feature of turbulence and is known as the turbulent/non-turbulent interface (TNTI). The features of the TNTI in jet, wake and boundary-layer flows have been investigated widely (da Silva *et al.* 2014). The geometry (Sreenivasan & Meneveau 1986; Sreenivasan, Ramshankar & Meneveau 1989; da Silva & Pereira 2008; de Silva *et al.* 2013), scaling (Holzner *et al.* 2007, 2008; Wolf *et al.* 2012; Davidson 2015), dynamics (Holzner *et al.* 2007, 2008; da Silva & dos Reis 2011; Taveira & da Silva 2013) of the TNTI and conditional statistics related to the TNTI (Bisset, Hunt & Rogers 2002; Westerweel *et al.* 2009) are the key characteristics that draw most researchers' attention. Studies on the TNTI can shed light on the turbulent entrainment process, i.e., the development of turbulence. Also, the TNTI is the imprint of vortical structures beneath, and thus can be an indicator of these vortical structures. This implies that the TNTI plays a role in revealing the physics underlying boundary layers.

Almost all previous TNTI-related investigations focused on low-speed flows, although the objective of this research field has expanded to the supersonic domain recently (Jahanbakhshi, Vaghefi & Madnia 2015; Vaghefi & Madnia 2015; Jahanbakhshi & Madnia 2016; Zhuang *et al.* 2018*a*). This offers a chance to acquire new information about the SWBLI phenomenon by examining features of the TNTI in SWBLI flows, which is a topic that has not been explored yet. With such knowledge, it is possible to further improve our insight into the SWBLI phenomenon and provide a better explanation of this classic issue. Thus, it is necessary to study the evolution of the TNTI in SWBLI flows.

In this paper, an experimental study on a compression ramp shock wave/turbulent boundary-layer interaction (CR-SWBLI) flow with an incoming Mach number of 2.83 is presented. To achieve images of high spatiotemporal resolution, the ice-cluster-based planar laser scattering (IC-PLS) technique is applied at the streamwise-vertical mid-plane of the test model. Then, the box-counting method is applied to the extracted TNTI. The results show that the TNTI after the interaction is self-similar, with a fractal dimension of 2.22, which is distinct from the value of the zero-pressure-gradient turbulent boundary layer (Zhuang *et al.* 2018*a*), $D_f = 2.31$. Additionally, the fractal features of the TNTI at various streamwise positions are compared.

2. Method

2.1. *Experimental set-up*

The experiments were conducted in a supersonic blowdown wind tunnel at Nanjing University of Aeronautics and Astronautics. The incoming boundary-layer condition is matched to a recent experimental study of Zhuang *et al.* (2018*a*), featuring a free-stream Mach number of $M_0 = 2.83$, a thickness of $\delta_0 = 11.6$ mm and a Reynolds number (δ_0 based) of $Re_{\delta_0} = 9.14 \times 10^4$. The actual incoming flow parameters of this study are summarised in table 1. A ramp-on-plate model with a width of $W = 150$ mm and a deflection angle of $\vartheta = 25°$ is employed, resulting in a separation bubble and a separation–reattachment shock wave system (see figure 1). The IC-PLS visualisation technique, details of which will be given in the next subsection, is deployed at the mid-plane of the test model. To avoid complexity in the vicinity of the separation bubble, this study focuses on TNTIs after reattachment. Thus, the region of interest, indicated by the yellow box in figure 1, features a rectangular area of height and

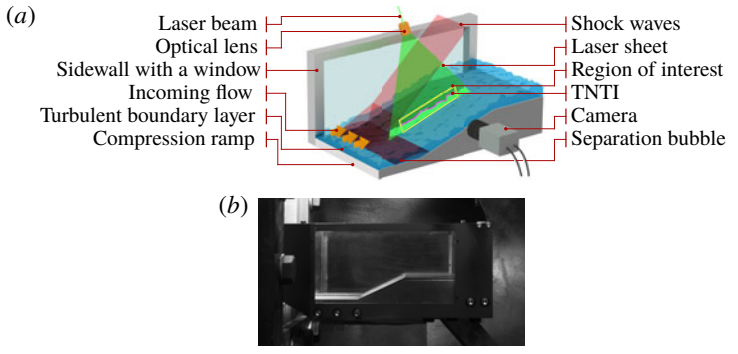

FIGURE 1. (*a*) Illustration of the experimental facilities. IC-PLS images are acquired at the streamwise-vertical (X–Y) centreplane. One sidewall and half of the shock waves are omitted for clarity. Drawing not to scale. (*b*) Image of the experimental model.

M_0 (U_0/c)	Re_{δ_0} ($U_0\delta_0/\upsilon$)	U_0 (m s^{-1})	δ_0 (mm)	η_0 (μm)	λ_0 (mm)	$T_{stag.}$ (k)	$P_{stag.}$ (Pa)	$\phi_{stag.}$ (%)
2.83	9.14×10^4	616.9	11.69	12.5	0.385	307.2	1.02×10^5	100

TABLE 1. Main aerodynamic parameters of the incoming flow. (M_∞, Re_{δ_0}, U_∞, δ_0, η_0, λ_0, $T_{stag.}$, $P_{stag.}$ and $\phi_{stag.}$ stand for the free-stream Mach number, the Reynolds number based on the incoming boundary-layer thickness, the free-stream speed, the incoming boundary-layer thickness, the Kolmogorov microscale, the Taylor microscale calculated near the interface, the stagnation temperature, the stagnation pressure and the relative humidity in stagnated air).

width $1.6\delta_0$ and $3\delta_0$, respectively, located $1.5\delta_0$ behind the corner, downstream of the separation bubble (Settles, Fitzpatrick & Bogdonoff 1979; Loginov, Adams & Zheltovodov 2006).

2.2. *Ice-cluster-based planar laser scattering (IC-PLS) technique*

The IC-PLS technique is a contactless flow visualisation technique characterised by high temporal resolution and has been applied successfully in supersonic airflow-related studies (Smith & Smits 1995; Poggie *et al.* 2004). While expanding in the nozzle, the temperature of airflow falls substantially, and water molecules deposit inside and accumulate into small ice clusters, which act as tracers (Wegener & Pouring 1964). A thin laser sheet is introduced to the plane of interest and illuminates a slice of the flow field. The flow pattern at this cross-section is illustrated by laser scattering of ice clusters. Although this method is not new, with developments on each of the components its spatial resolution has improved significantly (Zhuang *et al.* 2018*c*). This provides a solid base for studies on the geometry of the TNTI, which requires data at various length scales.

A digital single-lens reflex camera (Canon 1Dx Mark II) is used in the experiment, resulting in images with a spatial resolution of 35.1 μm pixel^{-1}, or 2.81 η_0 pixel^{-1}. The Beamtech Vlite-380 pulsed laser (Nd:YAG laser with a wavelength of 532 nm and a pulse duration of 10 ns) together with a laser light arm and an optical lens provide the illuminating laser sheet. The short pulse duration indicates a short

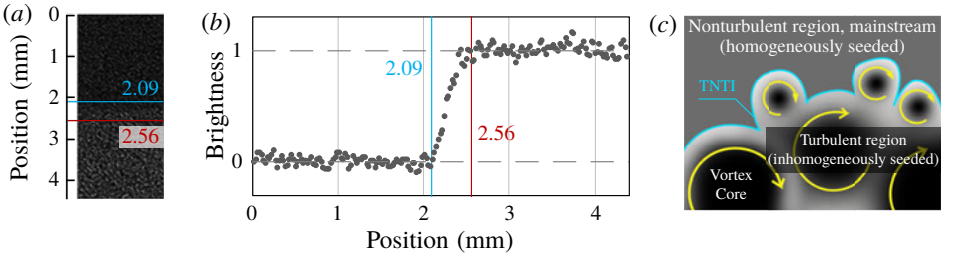

FIGURE 2. (*a*) An IC-PLS sample showing the relaxation of particles while passing through a shock wave. (*b*) Normalised brightness distribution in the vicinity of a shock wave. The distance between the blue and red lines is a measure of the relaxation length of the particles. (*c*) A sketch of the particle distribution near the interface between the turbulent region and the non-turbulent region. Brighter areas refer to places with a higher density of particles.

exposure time and thus freezes the flow effectively. The sampling frequency of the system is 7 Hz, which implies that acquired images are temporally uncorrelated. This technique offers an accessible scale range covering nearly three orders of magnitude, which allows the TNTI to be measured approximately at both scale ends of the turbulent boundary layer (that is, the levels of δ_0 and η_0). Such a wide range provides a good chance of observing whether any self-similarity exists.

Figure 2(*a*) shows a sample IC-PLS image of a shock wave in this experiment. The image brightness represents the intensity of scattering and thus shows the local flow density if the ice clusters can follow the fluid faithfully. However, due to the hysteresis effect, it will take a certain period for tracers to catch up with disturbed flows. This time period is known as the relaxation time τ_r, which is an important feature for flow tracers. Considering that the thickness of the shock wave is negligible, the relaxation distance $L = 0.47$ mm is acquired by measuring the brightness slope after the shock wave (demonstrated in figure 2*b*). Then, the relaxation time $\tau_r = 1.55$ μs is obtained from the known incoming flow speed. Also, according to Zhao *et al.* (2009), the typical diameters of ice clusters are approximately 500 nm, which is two orders of magnitude smaller than the projected scale of a single pixel on the sampling plane (35.1 μm), and thus is small enough to depict the flow field.

Vortical structures are the basic elements of turbulent flows. According to Samimy & Lele (1991), only when the Stokes number is smaller than 0.1 can the particles in compressible turbulent boundary layers trace faithfully. Thus, the following equation is acquired:

$$S_{tk} = \frac{\tau u}{l} \leqslant 0.1, \tag{2.1}$$

where τ is the relaxation time of the particles, u is the speed of flow well away from the obstacle and l is the scale of obstacle. In this test, the relaxation time of ice clusters is 1.55 μs, and the value of u can be chosen as $0.1U_0$ (Adrian, Meinhart & Tomkins 2000). Considering that flow in the vortex moves approximately around its centreline, the tracers have to fight against the centrifugal force to enter the core regions of the vortex. This indicates that it is reasonable to treat the vortices in turbulence as obstacles in (2.1); thus, l should be the diameter of a vortex at the intersection plane perpendicular to the centreline, since vortices are tube-like. Thus,

the critical value of $l_c = 0.95$ mm is achieved, and ice clusters cannot follow the flow in vortices with l smaller than 0.95 mm. Considering this critical value is only one order of magnitude smaller than the boundary-layer thickness, it is considered a large value, which means that particles in the turbulent region have a high probability of not following the flow faithfully. Consequently, as shown in figure 2(*c*), ice clusters accumulate in spaces between vortices and the edge of the turbulent region, indicating that the turbulent region is bounded by areas of high ice-cluster density (bright regions). This provides the basis for using this technique to detect the TNTI.

The turbulent region is bounded by bright bands, which allows the application of the brightness threshold TNTI detection method. This method has been widely used in the detection of the TNTI (Sreenivasan & Meneveau 1986; Prasad & Sreenivasan 1989, 1990). The normalised brightness threshold value used in this study is 0.16 (0 and 1 refer to black and white, respectively) and no other values are tested since it is a weak factor on the final fractal dimension (Sreenivasan & Meneveau 1986; Prasad & Sreenivasan 1990; Sreenivasan 1991; Mathew & Basu 2002; Westerweel *et al.* 2009; de Silva *et al.* 2013). The results agree well with visual inspection; samples are shown in the next section.

2.3. *Fractal analysis and the box-count method*

TNTIs, which are imprints of complex vortices underneath, are highly convoluted. The convolutions exist at a large length-scale range due to the hierarchical structures in high-Reynolds-number turbulence. As a result, the geometry of TNTIs cannot be built up by traditional means without introducing dubious assertions, whereas geometry at various scales is a natural attribute of fractals (Mandelbrot 1982). To test the fractal feature of the TNTI, the box-counting algorithm (Liebovitch & Toth 1989) in the program of FracLac (Karperien, A., FracLac for ImageJ, version 2.5. https://imagej.nih.gov/ij/plugins/fraclac/FLHelp/Introduction.htm. 1999–2013) built for the ImageJ software package (Schneider, Rasband & Eliceiri 2012) is applied. The box-counting algorithm tests the geometry of objects under different observation scales by breaking objects into pieces of box shape on a scale hierarchy and finding the relationship between the number of pieces and the corresponding length scale. In this test, the value of $N(r)$, the minimum number of boxes needed to cover the target interface, is counted in the scale range η_0–δ_0. The gross streamwise length of the TNTI extracted from different pictures is larger than $100\delta_0$, a sufficient length for reliable results.

3. Results

Figure 3(*a*) shows a general flow pattern of the aft portion of the CR-SWBLI flow. The green box outlines the region of interest introduced in § 2, which is further divided into three equal regions with lengths of δ_0 and heights of $1.6\delta_0$ to provide a more fundamental insight into the evolution of the fractal features of the TNTI during the relaxation process. Regions A, B and C refer to the upstream, middle and downstream subregions, respectively. Figure 3(*b*) compares the mean wall pressure of the present study and a previous CR-SWBLI flow of similar flow parameters (Settles *et al.* 1979). In general, their normalised pressure distributions overlap with each other.

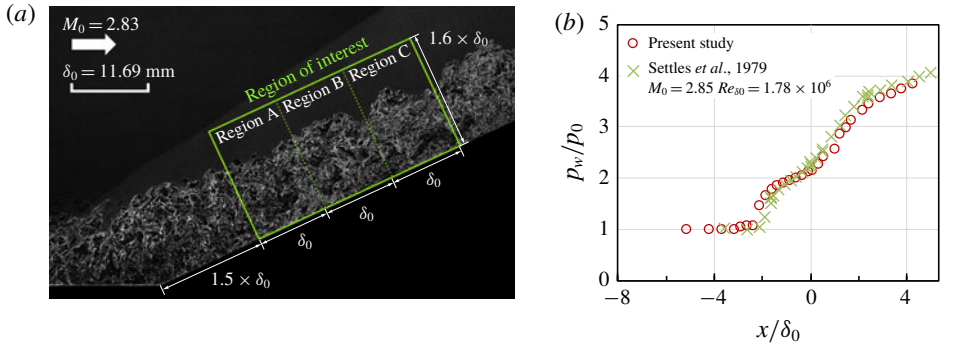

FIGURE 3. (*a*) Sample image of the general flow pattern that shows the region of interest and three subregions. (*b*) Mean wall pressure of the present study and one previous study of similar flow conditions.

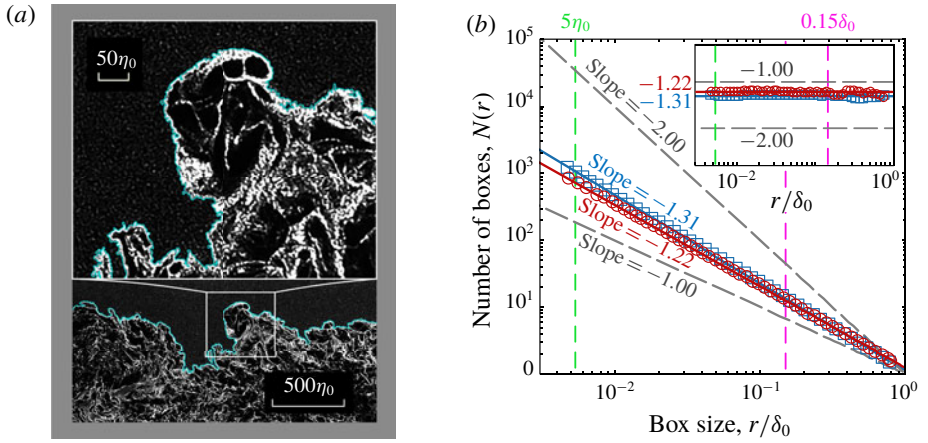

FIGURE 4. (*a*) An IC-PLS sample with its close-up view. The brightness indicates the concentration of ice clusters. The cyan line shows the position of the TNTI. (*b*) Log–log graph of the number of boxes needed to cover the interface at various box sizes. Circles refer to the TNTI after the reattachment in a SWBLI flow, and squares refer to the TNTI of the undisturbed boundary layer (Zhuang *et al.* 2018*a*). For better comparison, two dashed grey lines show slopes of −1 and −2. Vertical lines show the limits used for each data set.

3.1. *General evolution on TNTI fractal features after SWBLI*

A fractal analysis of the TNTIs, which are obtained after the reattachment, is conducted to explore the evolution of the fractal features of the TNTI in the SWBLI flow. Figure 4(*a*) shows an IC-PLS sample with its close-up view. The cyan line is the detected TNTI, which agrees well with the visual inspection and lays a solid foundation for the fractal-related studies. Also, the velocity profile of the boundary layer after the interaction varies during the relaxation process, which means the parameters of the boundary layer at different streamwise positions vary slightly (Loginov *et al.* 2006). However, the existence and fractal dimension of self-similarity

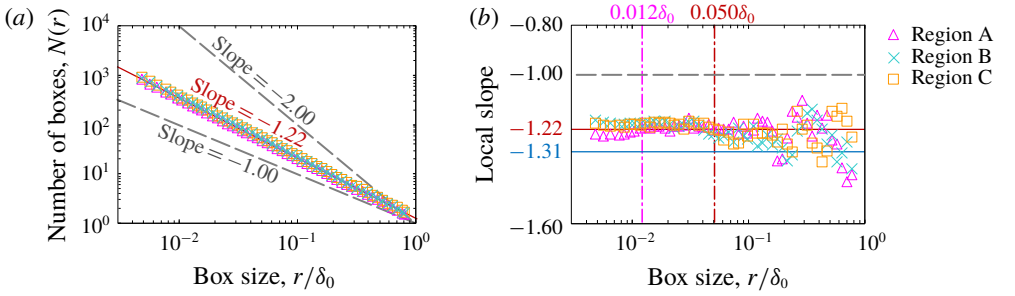

FIGURE 5. According to the streamwise position, the field of view is divided into three equal portions. The TNTIs acquired in regions A, B and C are indicated by the triangles, crosses and squares, respectively. (*a*) Log–log graph of the number of boxes needed to cover the interface at three subregions for various box sizes. (*b*) Semilog graph of the local slope for various box sizes. For better comparison, two dashed grey lines showing slopes of −1 and −2, one red solid line showing a slope of −1.22 and one blue solid line showing a slope of −1.31 are plotted.

are not related to the reference length scale. Thus, to simplify the study, the incoming parameters (δ_0 and η_0) are designated as uniform parameters after the interaction.

Figure 4(*b*) compares the log–log plots of the box number at different measurement scales before (Zhuang *et al.* 2018*a*) and after the interaction. An inset showing the local slope distribution, which is obtained by calculating the logarithmic derivative with the centred finite difference method, is shown in this figure. The red and blue solid lines provide references of the local slope values of −1.22 and −1.31, respectively. On comparing the distribution of circles and the red solid line, it is clear that they overlap each other in a wide scale range, which implies the presence of self-similarity of TNTIs after the interaction. Moreover, there exists no evident change of slope value in the vicinity of the lower scale end. On the other hand, the local slope near the upper scale is not reliable due to the lack of samples in this region, which is a disadvantage of the box-counting method. Thus, considering the additive law, the TNTI after the interaction is a self-similar fractal with a fractal dimension of 2.22 (with a standard error of 0.003) in the scale range from $3.8\eta_0$ to $0.15\delta_0$.

3.2. *Evolution of TNTI fractal features during relaxation*

Figures 5(*a*,*b*) show separately the log–log plot of the box-counting results of TNTIs in the three subregions and the corresponding distributions of the local slope. The red and blue solid lines in this figure indicate local slope values of −1.22 and −1.31, respectively. As is presented in figure 5(*a*), the overall box number to box size relationships during the relaxation are quite similar. The three data sets generally overlap with the red solid line with slight deviations, implying the presence of self-similarity of the TNTIs acquired from the three subregions. The three-dimensional fractal dimensions of the TNTIs of regions A, B and C are calculated as 2.22, 2.22 and 2.21, respectively, according to the additive law with standard error values of 0.003, 0.005, 0.004 in the scale range from $3.8\eta_0$ to $0.15\delta_0$. The data divergence, caused by a decrease in the number of boxes counted, occurs near the upper bound for all three regions. The upper bound is not taken into consideration in the subsequent analysis.

Figure 5(*b*) shows the detailed local slope distributions, which are linearly and negatively correlated to the fractal dimension distributions at various length scales. It can be observed that although the statistics of the fractal features of these three regions are very much alike, their distributions present some differences. The local slope of region A is lower, which implies a larger fractal dimension, at the lower bound (smaller than $0.012\delta_0$) and stays slightly larger than the general value of -1.22 in the remaining scale range. On the other hand, the local slope distributions of regions B and C are similar: a critical box size of $0.05\delta_0$ divides these distributions into two parts, the local slopes in the upper portion are obviously lower than the general value, and those in the lower portion are slightly higher than the general value.

4. Discussion

As presented in figure 4, although the TNTIs acquired before and after the interaction both present obvious self-similarity, their fractal dimensions are distinct. The fractal dimension value of the TNTI falls after reattachment, indicating the blunting of the contorted interface over a wide scale range. This difference is demonstrated more directly in the supplementary material (available at https://doi.org/10.1017/jfm.2019.299), where TNTIs acquired from the incoming flow and the boundary layer after reattachment are both presented with their partial enlargements. The change of fractal dimension implies the effect of SWBLI on the hierarchical vortical structures, since the TNTI is the imprint of the vortical structures underneath. A blunter interface indicates an increased homogeneity of vortices near the interface, which agrees with the result reported by Zhuang *et al.* (2018*b*). Also, the decrease in the fractal dimension value of the TNTI implies a reduction in the area of the interface, and thus leads to a change in the development process of boundary layer (Sreenivasan *et al.* 1989).

Furthermore, comparing the local slope distributions of TNTIs of the incoming flow and boundary layer in the three subregions, some insights into the flow interaction and the subsequent relaxation can be revealed. First, during the interaction, although all vortical structures are affected by the drastic shearing and mixing effect from the separation bubble and the Görtler-like vortices, the impacts on vortical structures of different scales are not the same. Large vortical structures are more readily affected than small ones, as the change of local slope of the TNTI in region A is larger in the large-scale range than that in the small-scale range. Second, during the relaxation process, the local slope in the small-scale range rises, yet in the large-scale range it falls, indicating further smoothing of small-scale vortical structures and contortion of large-scale vortical structures. This may be attributed to the effect of the Görtler-like vortices, which dominate the boundary layer during the relaxation after reattachment (Zhuang *et al.* 2017). These quasi-streamwise, large-scale 3D vortices create new large-scale vortices in the macroperspective and further mix small vortices in the microperspective.

In conclusion, to provide insights into the classic SWBLI issue, the evolution of fractal features of the TNTI in a separated CR-SWBLI flow is experimentally investigated. Results show that the TNTI acquired after the interaction is self-similar, with a general fractal dimension of 2.22 over a wide scale range, which is smaller than that of the incoming boundary layer if we ignore the potential difference between particles in these two studies. Also, by comparing the fractal characters of the TNTIs of the incoming flow and boundary layer of regions A, B and C, a deeper

understanding of the effect of both the interaction and the relaxation is obtained. Such studies offer a novel perspective for this classic research field and may be valuable in promoting our understanding of the underlying physics.

Supplementary material

Supplementary material is available at https://doi.org/10.1017/jfm.2019.299.

Acknowledgements

This work is jointly funded by the National Natural Science Foundation of P.R. China through grant nos 11532007 and 11502111 and the Jiangsu '333' Program for High Level Talent through grant no. BRA2018031. We thank the editor, the reviewers and Mr M. Hennessey-Wesen for their valuable work in improving the quality of the paper.

References

ADAMSON, T. C. JR & MESSITER, A. F. 1980 Analysis of two-dimensional interactions between shock waves and boundary layers. *Annu. Rev. Fluid Mech.* **12** (1), 103–138.

ADRIAN, R. J., MEINHART, C. D. & TOMKINS, C. D. 2000 Vortex organization in the outer region of the turbulent boundary layer. *J. Fluid Mech.* **422**, 1–54.

BABINSKY, H. & HARVEY, J. K. 2011 *Shock Wave-Boundary-Layer Interactions*, vol. 32. Cambridge University Press.

BISSET, D. K., HUNT, J. C. R. & ROGERS, M. M. 2002 The turbulent/non-turbulent interface bounding a far wake. *J. Fluid Mech.* **451**, 383–410.

CORRSIN, S. & KISTLER, A. L. 1954 The free-stream boundaries of turbulent flows. NACA Tech. Rep. 3133.

DAVIDSON, P. 2015 *Turbulence: An Introduction for Scientists and Engineers*. Oxford University Press.

DOLLING, D. S. 2001 Fifty years of shock-wave/boundary-layer interaction research: what next? *AIAA J.* **39** (8), 1517–1531.

FERRI, A. 1940 Experimental results with airfoils tested in the high-speed tunnel at Guidonia. NACA Tech. Rep. 946.

GAITONDE, D. V. 2015 Progress in shock wave/boundary layer interactions. *Prog. Aerosp. Sci.* (72), 80–99.

HOLZNER, M., LIBERZON, A., NIKITIN, N., KINZELBACH, W. & TSINOBER, A. 2007 Small-scale aspects of flows in proximity of the turbulent/nonturbulent interface. *Phys. Fluids* **19** (7), 071702.

HOLZNER, M., LIBERZON, A., NIKITIN, N., LÜTHI, B., KINZELBACH, W. & TSINOBER, A. 2008 A Lagrangian investigation of the small-scale features of turbulent entrainment through particle tracking and direct numerical simulation. *J. Fluid Mech.* **598**, 465–475.

JAHANBAKHSHI, R. & MADNIA, C. K. 2016 Entrainment in a compressible turbulent shear layer. *J. Fluid Mech.* **797**, 564–603.

JAHANBAKHSHI, R., VAGHEFI, N. S. & MADNIA, C. K. 2015 Baroclinic vorticity generation near the turbulent/non-turbulent interface in a compressible shear layer. *Phys. Fluids* **27** (10), 105105.

LIEBOVITCH, L. S. & TOTH, T. 1989 A fast algorithm to determine fractal dimensions by box counting. *Phys. Lett.* A **141** (89), 386–390.

LOGINOV, M. S., ADAMS, N. A. & ZHELTOVODOV, A. A. 2006 Large-eddy simulation of shock-wave/turbulent-boundary-layer interaction. *J. Fluid Mech.* **565**, 135–169.

MANDELBROT, B. B. 1982 *The Fractal Geometry of Nature*, vol. 1. WH Freeman.

MATHEW, J. & BASU, A. J. 2002 Some characteristics of entrainment at a cylindrical turbulence boundary. *Phys. Fluids* **14** (7), 2065–2072.

POGGIE, J., ERBLAND, P. J., SMITS, A. J. & MILES, R. B. 2004 Quantitative visualization of compressible turbulent shear flows using condensate-enhanced Rayleigh scattering. *Exp. Fluids* **37** (3), 438–454.

PRASAD, R. R. & SREENIVASAN, K. R. 1989 Scalar interfaces in digital images of turbulent flows. *Exp. Fluids* **7** (4), 259–264.

PRASAD, R. R. & SREENIVASAN, K. R. 1990 The measurement and interpretation of fractal dimensions of the scalar interface in turbulent flows. *Phys. Fluids* A **2** (5), 792–807.

SAMIMY, M. & LELE, S. K. 1991 Motion of particles with inertia in a compressible free shear layer. *Phys. Fluids* A **3** (8), 1915–1923.

SCHNEIDER, C. A., RASBAND, W. S. & ELICEIRI, K. W. 2012 NIH Image to ImageJ: 25 years of image analysis. *Nat. Meth.* **9** (7), 671–675.

SETTLES, G. S., FITZPATRICK, T. J. & BOGDONOFF, S. M. 1979 Detailed study of attached and separated compression corner flowfields in high Reynolds number supersonic flow. *AIAA J.* **17** (6), 579–585.

DA SILVA, C. B., HUNT, J. C. R., EAMES, I. & WESTERWEEL, J. 2014 Interfacial layers between regions of different turbulence intensity. *Annu. Rev. Fluid Mech.* **46**, 567–590.

DA SILVA, C. B. & PEREIRA, J. C. F. 2008 Invariants of the velocity-gradient, rate-of-strain, and rate-of-rotation tensors across the turbulent/nonturbulent interface in jets. *Phys. Fluids* **20** (5), 055101.

DA SILVA, C. B. & DOS REIS, R. J. N. 2011 The role of coherent vortices near the turbulent/non-turbulent interface in a planar jet. *Phil. Trans. R. Soc. Lond.* A **369** (1937), 738–753.

DE SILVA, C. M., PHILIP, J., CHAUHAN, K., MENEVEAU, C. & MARUSIC, I. 2013 Multiscale geometry and scaling of the turbulent–nonturbulent interface in high Reynolds number boundary layers. *Phys. Rev. Lett.* **111** (4), 044501.

SMITH, M. W. & SMITS, A. J. 1995 Visualization of the structure of supersonic turbulent boundary layers. *Exp. Fluids* **18** (4), 288–302.

SMITS, A. J. & DUSSAUGE, J.-P. 2006 *Turbulent Shear Layers in Supersonic Flow*. Springer Science & Business Media.

SREENIVASAN, K_R. 1991 Fractals and multifractals in fluid turbulence. *Annu. Rev. Fluid Mech.* **23** (1), 539–604.

SREENIVASAN, K. R. & MENEVEAU, C. J. F. M. 1986 The fractal facets of turbulence. *J. Fluid Mech.* **173**, 357–386.

SREENIVASAN, K. R., RAMSHANKAR, R. & MENEVEAU, C. H. 1989 Mixing, entrainment and fractal dimensions of surfaces in turbulent flows. *Proc. R. Soc. Lond.* A **421** (1860), 79–108.

TAVEIRA, R. R. & DA SILVA, C. B. 2013 Kinetic energy budgets near the turbulent/nonturbulent interface in jets. *Phys. Fluids* **25** (1), 015114.

VAGHEFI, N. S. & MADNIA, C. K. 2015 Local flow topology and velocity gradient invariants in compressible turbulent mixing layer. *J. Fluid Mech.* **774**, 67–94.

WEGENER, P. P. & POURING, A. A. 1964 Experiments on condensation of water vapor by homogeneous nucleation in nozzles. *Phys. Fluids* **7** (3), 352–361.

WESTERWEEL, J., FUKUSHIMA, C., PEDERSEN, J. M. & HUNT, J. C. R. 2009 Momentum and scalar transport at the turbulent/non-turbulent interface of a jet. *J. Fluid Mech.* **631**, 199–230.

WOLF, M., LÜTHI, B., HOLZNER, M., KRUG, D., KINZELBACH, W. & TSINOBER, A. 2012 Investigations on the local entrainment velocity in a turbulent jet. *Phys. Fluids* **24** (10), 105110.

ZHAO, Y., YI, S., TIAN, L. & CHENG, Z. 2009 Supersonic flow imaging via nanoparticles. *Sci. China Ser. E: Technol. Sci.* **52** (12), 3640–3648.

ZHELTOVODOV, A. 1996 Shock waves/turbulent boundary-layer interactions-fundamental studies and applications. AIAA Paper 96-1977.

ZHUANG, Y., TAN, H., HUANG, H., LIU, Y. & ZHANG, Y. 2018*a* Fractal characteristics of turbulent–non-turbulent interface in supersonic turbulent boundary layers. *J. Fluid Mech.* **843**, R2.

ZHUANG, Y., TAN, H.-J., LI, X., GUO, Y.-J. & SHENG, F.-J. 2018*b* Evolution of coherent vortical structures in a shock wave/turbulent boundary-layer interaction flow. *Phys. Fluids* **30** (11), 111702.

ZHUANG, Y., TAN, H.-J., LI, X., SHENG, F.-J. & ZHANG, Y.-C. 2018*c* Letter: Görtler-like vortices in an impinging shock wave/turbulent boundary layer interaction flow. *Phys. Fluids* **30** (6), 061702.

ZHUANG, Y., TAN, H.-J., LIU, Y.-Z., ZHANG, Y.-C. & LING, Y. 2017 High resolution visualization of Görtler-like vortices in supersonic compression ramp flow. *J. Vis.* **20** (3), 505–508.